



**Skin-interfaced soft microfluidics systems with modular and reusable electronics for in-situ capacitive sensing of sweat loss, rate and conductivity**

Journal:	<i>Lab on a Chip</i>
Manuscript ID	LC-ART-07-2020-000705.R1
Article Type:	Paper
Date Submitted by the Author:	02-Oct-2020
Complete List of Authors:	<p>Hourlier-Fargette, Aurélie; Northwestern University, Querrey Simpson Institute for Bioelectronics; Northwestern University, Department of Materials Science and Engineering; Université de Strasbourg, CNRS, Institut Charles Sadron, UPR22</p> <p>Schon, Stéphanie; Northwestern University, Querrey Simpson Institute for Bioelectronics; Northwestern University, Department of Materials Science and Engineering; ETH Zürich, Department of Mechanical and Process Engineering</p> <p>Xue, Yeguang; Northwestern University, Department of Mechanical Engineering</p> <p>Avila, Raudel; Northwestern University, Department of Mechanical Engineering</p> <p>Li, Weihua; Northwestern University, Querrey Simpson Institute for Bioelectronics; Epicore Biosystems, Inc</p> <p>Gao, Yiwei; Northwestern University, Querrey Simpson Institute for Bioelectronics; Northwestern University, Department of Biomedical Engineering</p> <p>Liu, Claire; Northwestern University, Querrey Simpson Institute for Bioelectronics; Northwestern University, Department of Biomedical Engineering</p> <p>Kim, Sung Bong; Northwestern University, Querrey Simpson Institute for Bioelectronics; University of Illinois at Urbana-Champaign, Department of Materials Science and Engineering and Materials Research Laboratory</p> <p>Raj, Milan; Northwestern University, Querrey Simpson Institute for Bioelectronics; Epicore Biosystems, Inc</p> <p>Fields, Kelsey; Northwestern University, Querrey Simpson Institute for Bioelectronics; Northwestern University, Department of Materials Science and Engineering</p> <p>Parsons, Blake; Northwestern University, Querrey Simpson Institute for Bioelectronics; Northwestern University, Department of Biomedical Engineering</p> <p>Lee, KunHyuck; Northwestern University, Querrey Simpson Institute for Bioelectronics; Northwestern University, Department of Materials Science and Engineering</p> <p>Lee, Jong Yoon; Northwestern University, Querrey Simpson Institute for Bioelectronics; Sibel Inc</p> <p>Chung, Ha Uk; Northwestern University, Querrey Simpson Institute for Bioelectronics; Northwestern University, Department of Electrical and</p>

	<p>Computer Engineering; Sibel Inc  Lee, Stephen ; Northwestern University, Querrey Simpson Institute for Bioelectronics; Epicore Biosystems, Inc  Johnson, Michael; Northwestern University, Querrey Simpson Institute for Bioelectronics; Northwestern University, Department of Biomedical Engineering  Bandodkar, Amay; Northwestern University, Querrey Simpson Institute for Bioelectronics; Northwestern University, Department of Materials Science and Engineering  Gutruf, Philipp; Northwestern University, Querrey Simpson Institute for Bioelectronics; The University of Arizona, Departments of Biomedical Engineering, Electrical and Computer Engineering, Bio5 Institute, Neuroscience GIDP  Model, Jeffrey; Northwestern University, Querrey Simpson Institute for Bioelectronics; Epicore Biosystems, Inc  Aranyosi, Alexander; Northwestern University, Querrey Simpson Institute for Bioelectronics; Epicore Biosystems, Inc  Choi, Jungil; Northwestern University, Querrey Simpson Institute for Bioelectronics; Kookmin University, School of Mechanical Engineering  Ray, Tyler; Northwestern University, Querrey Simpson Institute for Bioelectronics; University of Hawai'i at Manoa, Department of Mechanical Engineering  Ghaffari, Roozbeh; Northwestern University, Querrey Simpson Institute for Bioelectronics; Epicore Biosystems, Inc; Northwestern University, Department of Biomedical Engineering  Huang, Yonggang; Northwestern University, Querrey Simpson Institute for Bioelectronics; Northwestern University, Department of Mechanical Engineering; Northwestern University, Department of Materials Science and Engineering; Northwestern University, Department of Civil and Environmental Engineering  Rogers, John; Northwestern University, Querrey Simpson Institute for Bioelectronics; Northwestern University, Department of Materials Science and Engineering, Department of Biomedical Engineering, Department of Mechanical Engineering, Department of Electrical and Computer Engineering, Department of Chemistry ; Northwestern University  Feinberg School of Medicine, Neurological Surgery; Epicore Biosystems, Inc</p>

1 **Skin-interfaced soft microfluidics systems with modular and reusable electronics for in-**  
2 **situ capacitive sensing of sweat loss, rate and conductivity**

3

4 Aurélie Hourlier-Fargette<sup>1,2,3</sup>, Stéphanie Schon<sup>1,2,4</sup>, Yeguang Xue<sup>5</sup>, Raudel Avila<sup>5</sup>, Weihua  
5 Li<sup>1,6</sup>, Yiwei Gao<sup>1,7</sup>, Claire Liu<sup>1,7</sup>, Sung Bong Kim<sup>1,8</sup>, Milan S. Raj<sup>1,6</sup>, Kelsey B. Fields<sup>1,2</sup>,  
6 Blake V. Parsons<sup>1,7</sup>, KunHyuck Lee<sup>1,2</sup>, Jong Yoon Lee<sup>1,9</sup>, Ha Uk Chung<sup>1,9,10</sup>, Stephen P.  
7 Lee<sup>1,6</sup>, Michael Johnson<sup>1,7</sup>, Amay J. Bandodkar<sup>1,2</sup>, Philipp Gutruf<sup>1,11</sup>, Jeffrey B. Model<sup>1,6</sup>,  
8 Alexander J. Aranyosi<sup>1,6</sup>, Jungil Choi<sup>1,12</sup>, Tyler R. Ray<sup>1,13</sup>, Roozbeh Ghaffari<sup>1,6,7</sup>, Yonggang  
9 Huang<sup>1,2,5,14</sup>, and John A. Rogers<sup>1,2,5,6,7,10,15,16\*</sup>

10

11 <sup>1</sup> Querrey Simpson Institute for Bioelectronics, Northwestern University, Evanston, IL 60208,  
12 USA.

13 <sup>2</sup> Department of Materials Science and Engineering, Northwestern University, Evanston, IL  
14 60208, USA.

15 <sup>3</sup> Université de Strasbourg, CNRS, Institut Charles Sadron UPR22, F-67000 Strasbourg,  
16 France.

17 <sup>4</sup> Department of Mechanical and Process Engineering ETH Zurich, CH-8092 Zurich,  
18 Switzerland

19 <sup>5</sup> Department of Mechanical Engineering, Northwestern University, Evanston, IL 60208,  
20 USA

21 <sup>6</sup> Epicore Biosystems, Inc. Cambridge, MA 02139, USA.

22 <sup>7</sup> Department of Biomedical Engineering, Northwestern University, Evanston, IL 60208,  
23 USA.

24 <sup>8</sup> Department of Materials Science and Engineering and Materials Research Laboratory,  
25 University of Illinois at Urbana-Champaign, Urbana, IL 61801, USA.

26 <sup>9</sup> Sibel Inc, Evanston, IL 60201, USA.

27 <sup>10</sup> Department of Electrical and Computer Engineering, Northwestern University, Evanston,  
28 IL, USA.

29 <sup>11</sup> Departments of Biomedical Engineering, Electrical and Computer Engineering, Bio5  
30 Institute, Neuroscience GIDP, The University of Arizona, Tucson, 85721

31 <sup>12</sup> School of Mechanical Engineering, Kookmin University, Seoul 02707, South Korea

32 <sup>13</sup> Department of Mechanical Engineering, University of Hawai'i at Mānoa, Honolulu, HI  
33 96822, USA

34 <sup>14</sup> Department of Civil and Environmental Engineering, Northwestern University, Evanston,  
35 IL 60208, USA.

36 <sup>15</sup> Department of Chemistry, Northwestern University, Evanston, IL 60208, USA

37 <sup>16</sup> Department of Neurological Surgery, Feinberg School of Medicine, Northwestern  
38 University, Chicago, IL, USA.

39

40 \*To whom correspondence should be addressed. E-mail: [jrogers@northwestern.edu](mailto:jrogers@northwestern.edu)

41

42 Keywords: sweat, epidermal, capacitive measurements, microfluidics, wearables, sweat rate,  
43 sweat conductivity

**44 Abstract**

45 Important insights into human health can be obtained through the non-invasive collection  
46 and detailed analysis of sweat, a biofluid that contains a wide range of essential biomarkers.  
47 Skin-interfaced microfluidic platforms, characterized by soft materials and thin geometries,  
48 offer a collection of capabilities for in-situ capture, storage, and analysis of sweat and its  
49 constituents. In ambulatory uses cases, the ability to provide real-time feedback on sweat loss,  
50 rate and content, without visual inspection of the device, can be important. This paper  
51 introduces a low-profile skin-interfaced system that couples disposable microfluidic  
52 sampling devices with reusable ‘stick-on’ electrodes and wireless readout electronics that  
53 remain isolated from the sweat. An ultra-thin capping layer on the microfluidic platform  
54 permits high-sensitivity, contactless capacitive measurements of both sweat loss and  
55 electrolyte concentration. This architecture avoids the potential for corrosion of the sensing  
56 components and eliminates need for cleaning/sterilizing the electronics, thereby resulting in  
57 a cost-effective platform that is simple to use. Optimized electrode designs follow from a  
58 combination of extensive benchtop testing, analytical calculations and FEA simulations for  
59 two sensing configurations: (1) sweat rate and loss, and (2) sweat conductivity, which  
60 contains information about electrolyte content. Both configurations couple to a flexible,  
61 wireless electronics platform that digitizes and transmits information to Bluetooth-enabled  
62 devices. On-body field testing during physical exercise validates the performance of the  
63 system in scenarios of practical relevance to human health and performance.

64

65

## 66 **Introduction**

67 Sweat, as a biofluid that can be captured with completely non-invasive sampling procedures,  
68 can provide a valuable collection of data with relevance to human health<sup>1</sup>. Quantitative  
69 measurements of sweat constituents, such as electrolytes, metabolites and proteins, is  
70 particularly attractive in the context of medical diagnostics<sup>2,3</sup> and athletic performance<sup>4</sup>. Real-  
71 time analysis of sweat has immediate relevance in developing individualized hydration  
72 strategies to control electrolyte balance and to limit dehydration or overhydration during  
73 physical activity<sup>5</sup>. The utility of sweat for physiological monitoring is of rapidly growing  
74 interest due to the recent emergence of various classes of skin-interfaced digital devices that  
75 enable collection and analysis of sweat in the field, without the need for bulky laboratory  
76 instruments. Of specific interest are skin-like, or ‘epidermal’ microfluidic systems,  
77 sometimes referred to as epifluidic technologies, that consist of low-profile, micromolded  
78 channels embedded in soft elastomeric materials for in-situ measurements of sweat rate<sup>6</sup> and  
79 quantitative measurements of constituent concentrations through colorimetric<sup>7</sup>, fluorescence<sup>8</sup>,  
80 electrochemical<sup>9</sup>, or impedance-based<sup>10</sup> techniques. Such platforms can measure a variety of  
81 physiological parameters via eccrine sweat, across a range of practical applications, including  
82 uses in extreme environments<sup>11</sup>. These possibilities expand the capabilities and scope of those  
83 associated with traditional methods that utilize absorbent pads for sweat collection, with  
84 subsequent analysis performed in centralized facilities using conventional laboratory  
85 equipment<sup>4,12</sup>.

86 Electrolyte concentration in sweat is a key biomarker of interest, but its value is influenced  
87 by sweat rate due to the fundamental secretion and reabsorption mechanisms associated with

88 the sweat ducts.<sup>3, 13</sup> As such, measurements of both rate and electrolyte composition are  
89 necessary for conclusive analysis. Previous studies of sweat rate and electrolyte content often  
90 utilize visual observation within epifluidic devices, but such approaches require visual access  
91 and reference color charts to control for variable lighting conditions<sup>7, 14</sup>. Other continuous-  
92 mode embodiments provide real-time digital feedback on rate and/or electrolyte content  
93 through direct contact between the collected sweat and measurement electrodes<sup>10, 15, 16, 17</sup>.  
94 These platforms, however, have drawbacks such as limited robustness due to the presence of  
95 air bubbles at the electrode interface<sup>15</sup> and practical difficulties in cleaning and sterilizing the  
96 electrodes and associated electronics after each cycle of use. Most importantly, galvanic  
97 contacts with sweat require a protective encapsulation of the measurement electrodes with  
98 chemically inert metals such as gold to avoid corrosion reactions, thereby increasing  
99 manufacturing costs and preventing their deployment at scale. Here, we report a platform  
100 that utilizes non-contact electrodes capacitively coupled to the sweat as it travels through a  
101 microfluidic device. Combining this construct with Bluetooth-based electronics for data  
102 capture and wireless transmission enables continuous and real-time measurements of sweat  
103 conductivity and dynamics.

104 Capacitively-coupled approaches provide attractive means to measure fluid levels and to  
105 distinguish between different types of fluids. Dielectric properties of aqueous solutions have  
106 been studied widely in the literature especially in the mid-20<sup>th</sup> century<sup>18</sup>, but little information  
107 is available on the dielectric properties of human sweat<sup>19</sup>. Many types of microfluidic lab-  
108 on-a-chip technologies use capacitance-based measurements, to detect droplets size and  
109 speed<sup>20</sup>, to infer their content in the case of simple mixtures<sup>21</sup>, but also to provide quantitative

110 measurements in the context of biological materials including single cell analysis<sup>22,23</sup>. Some  
111 systems offer options in which electrodes contact fluid droplets directly, by measuring the  
112 double layer capacitance with two metal electrodes<sup>24</sup> or by evaluating the capacitance  
113 between a fluid channel and one metal electrode in its close vicinity with no electrical contact  
114 to the fluid<sup>25</sup>. More interestingly, non-contact measurements are possible with interdigitated  
115 electrode pairs<sup>20, 26</sup> in optimized geometries<sup>27</sup>, as described in several examples in the  
116 literature<sup>28-30</sup>. This paper describes adaptations and extensions of these basic concepts for the  
117 study of sweat using skin-interfaced microfluidic platforms. The approach optimizes the  
118 sensitivity through the use of ultra-thin capping layers on the channels as a sensing interface  
119 that offers sufficiently large changes in capacitance for accurate measurement using simple,  
120 compact readout electronics. Another important feature is in the electrical decoupling of  
121 the system from the underlying skin, to allow accurate, in situ measurements.<sup>31, 32</sup> A  
122 combination of experiments, analytical calculations and FEA simulations reveal the essential  
123 effects, to enable optimization of the measurement system and electrode geometries.  
124 Tailoring the layouts allows for measurement of both sweat rate and sweat conductivity from  
125 the capacitance values. A low-profile, custom readout circuit enables accurate wireless  
126 operation during human subject field studies on healthy volunteers.

127

## 128 **Results and discussion**

### 129 **Skin-interfaced capacitance-based electronics and microfluidics design**

130 The capacitance sensing module and microfluidics system consists of a collection of several  
131 sub-modules: (A) a soft skin-mounted disposable microfluidic system, (B) flexible,



132 repositionable and reusable electrodes, (C) a reusable electronics readout platform to digitize  
133 and transmit information collected by the electrodes wirelessly to a Bluetooth-enabled device  
134 (e.g. tablet), and (D) a rechargeable battery (Figure 1a). The geometries of modules (A) and  
135 (B) are optimized for measurements of sweat rate and conductivity. Modules (C) and (D) are  
136 the same for both types of measurements, as described in detail in the section on “electronics  
137 readout design”. Coupling between modules (B), (C) and (D) occurs through a magnetic  
138 interfacing scheme. Fully assembled devices for sweat rate and sweat conductivity  
139 measurements are shown in Figure 1b and 1c, with blue dye to enhance the visual contrast of  
140 the microfluidic channels. All components have low-profile, flexible designs, as shown in  
141 Figure 1d for the electronics readout, and electrodes (B) benefit from repositionable adhesive  
142 coupling to fluidics module (A), as illustrated in Figure 1e.

143 For measurements of sweat rate, module (A) consists of three layers of polymeric materials  
144 shown in Figure 1f: a thin polyester film (Mylar) as a uniform capping layer, a  
145 polydimethylsiloxane (PDMS) microfluidic layer fabricated via molding using soft  
146 lithography techniques to define a collection of microchannels, an inlet to the skin to allow  
147 entry of sweat and an outlet to the surrounding ambient air to suppress back-pressure. A  
148 medical-grade acrylic adhesive layer with an opening that aligns to the inlet bonds the device  
149 to the skin. Sweat enters through the inlet as a consequence of secretory fluidic pressures  
150 generated at the surface of the skin by eccrine sweat glands and fills progressively the  
151 channels<sup>33</sup>. The upper surface of the Mylar film serves as the foundation for a thin layer of  
152 silicone adhesive that allows repositionable contact to module (B), as shown in Figure 1e.  
153 Module (B) consists of a flexible polyimide (PI) / copper (Cu) clad sheet patterned with an

154 interdigitated array of electrodes. A set of magnets soldered to connection pads serve as an  
155 electrical and mechanical interface to module (C). Figure 1b shows the assembled device,  
156 and Figure 1f presents an exploded view to highlight the details of modules (A) and (B).  
157 Devices for measurement of sweat conductivity exploit similar stacks of materials, but with  
158 two important modifications to the geometry: (i) electrodes take the form of two pads that  
159 cover separate zones of the microchannel, with a small channel that connects the two, as  
160 inspired by designs for capacitively coupled contactless conductivity detection in other  
161 contexts<sup>34, 35</sup>; (ii) microchannels and Mylar film integrate on top of an additional flat layer of  
162 PDMS, with module (B) inserted in between to minimize the influence of the skin on the  
163 measurements. Module (B) presents electrodes on one side and an electrical ground plane of  
164 Cu on the other side, in between the electrodes and the skin. This plane, along with the  
165 electrodes, connects to module (C) using the magnetic coupling scheme described previously.  
166 Figure 1c shows the completed device, and Figure 1g presents an exploded view to highlight  
167 the details of parts (A) and (B). Fabrication protocols are in the Materials and Methods  
168 section. A thin, conformal coating of parylene-C, not shown in the illustration, protects the  
169 PI layer and electrodes in module (B) from moisture.

170

### 171 **Materials, mechanics, and design considerations for optimal capacitive coupling**

172 Capacitive coupling between the electrodes and microfluidic channels strongly depends on  
173 the distance between the liquid and electrodes, relevant for measurements of both rate<sup>20</sup> and  
174 conductivity<sup>35</sup>. As expected, the sensitivity improves with decreasing distance. The soft  
175 microfluidics platforms involve an assembly of two PDMS layers, one cast against a mold

176 that forms trenches, and another that is flat and mounts on top of first as a capping layer to  
177 define closed channels<sup>7, 14</sup>. The thickness of the capping layers in previously reported systems  
178 are in the range of ten to hundreds of micrometers. With PDMS (Young's modulus ~1-2  
179 MPa), mechanical collapse of the structures<sup>36, 37</sup> and wrinkling of the capping layer could  
180 limit the dimensions of the channels and the thickness of the capping layer. The use of Mylar  
181 (Young's modulus 1-3 GPa) instead of PDMS for the capping layer bypasses these  
182 limitations, where a seal to the PDMS channel layer occurs through covalent bonding<sup>38</sup>.  
183 Supplementary Figure S1a describes the assembly process. A 2.5  $\mu\text{m}$  thick Mylar film treated  
184 in a UVO-cleaner and immersed in a 2% volume solution of aminopropyltriethoxysilane  
185 (APTES) in DI water, subsequently washed, dried and placed on a sacrificial soft silicone  
186 elastomer layer facilitates handling and bonding during the assembly. Specifically, a UVO-  
187 treated PDMS channel layer laminated onto the Mylar sheet forms covalent bonding upon  
188 contact. Supplementary Figure S1b highlights considerations for different materials and  
189 thickness criteria. The bonding strength evaluated via mechanical testing (Figure S2)  
190 confirms the utility of the APTES functionalization approach<sup>38</sup> in achieving robust  
191 integration.

192

### 193 **Geometry optimization and benchtop testing of sweat rate**

194 Capacitive measurements of fluid levels are sensitive to the electrode geometry<sup>20,26,27</sup>. For  
195 on-body sweat measurements, an additional constraint is that the configuration must be  
196 highly sensitive to sweat in the channels adjacent to the electrodes, but insensitive to the  
197 underlying skin surface. The design parameters reported here involve interdigitated arrays of

198 copper (9  $\mu\text{m}$  in thickness) electrodes, with spacings  $G$ , widths  $W$ , lengths  $L = 1.5$  cm, and a  
199 total number of electrodes  $N$  across a total width of 1.5 cm (Figure 2a), on a layer of PI (25  
200  $\mu\text{m}$  in thickness) as a substrate. An analytical model for the capacitance of the interdigitated  
201 electrodes based on conformal mapping techniques<sup>39</sup> provides geometrical design guidelines.  
202 The capacitance is a function of number of electrodes  $N$ , metallization ratio  $\eta$  ( $\frac{W}{W+G}$ , defined  
203 in Figure 2a) and layer thickness to wavelength ratio  $t/\lambda$ , where  $\lambda = 2(W+G)$ . For fixed total  
204 device length  $L$  ( $L=N\lambda/2$ ), the independent variables can be redefined as  $\eta$ ,  $t$  and  $N$ . Figure  
205 2a shows the difference between the capacitance associated with the array when the material  
206 present at a distance  $t_{\text{PDMS}}$  (separated by a PDMS layer) changes from water to air, as a  
207 function of  $N$  with  $\eta=0.375$ . Results confirm that decreasing the separation of the electrodes  
208 from the material under test (i.e.  $t_{\text{PDMS}}$ ) increases the sensitivity. For a separation thickness  
209 fixed to the lowest value accessible given experimental constraints (corresponding to  
210 minimal capping layer and adhesive thicknesses), the number of electrodes that cover a  
211 domain of constant area only slightly affects sensitivity. The optimal value of  $N$  depends on  
212 considerations in the sensitivity of the system to the surrounding medium. Specifically, the  
213 measurement must be sensitive to the liquid inside the channels but not to the skin underneath.  
214 As a result,  $N$  is chosen to yield an effective sensing distance of several hundred microns  
215 around the electrodes, to approach the maximum sensitivity defined by the curve on Figure  
216 2a. The geometry used for benchtop analysis involves a photolithography mask with  $N=76$ ,  
217  $L=1.51$  cm,  $W=100$   $\mu\text{m}$  and  $G=100$   $\mu\text{m}$ , resulting in samples with  $W=75\pm 5$   $\mu\text{m}$  and  
218  $G=125\pm 5$   $\mu\text{m}$  after the etching process.

219 The thickness of the PDMS ( $t_{\text{PDMS}}$ ) underneath the electrodes must be sufficient to avoid  
220 significant contributions of the skin, while minimizing the overall thickness of the device.  
221 For a given optimal electrode geometry, the model constrains a few parameters ( $N = 76$ ,  
222  $\eta = 0.375$  and  $\lambda = 400 \mu\text{m}$ ) to explore the dependence on  $t_{\text{PDMS}}$ , as a means to evaluate  
223 the critical PDMS thickness beyond which the capacitance no longer changes depends on  
224  $t_{\text{PDMS}}$ . Fig. 2b shows the capacitance as a function of  $t_{\text{PDMS}}$  for an optimal electrodes  
225 geometry ( $N = 76$ ,  $\eta = 0.375$  and  $\lambda = 400 \mu\text{m}$ ) when in air at room temperature (red) and  
226 on skin (blue). Open symbols correspond to experiments and dashed lines to the analytical  
227 model. Capacitances are normalized by the value in the limit of large  $t_{\text{PDMS}}$ , to provide  
228 guidelines on the minimum  $t_{\text{PDMS}}$  for which contributions from the skin are at the level of a  
229 few percent. The raw data appears in Supplementary Figure S3. Supplementary Figure S4  
230 shows the full spectral results captured with the impedance analyzer. The frequency of 25  
231 kHz corresponds to a convenient value for the operation of the miniaturized capacitance-to-  
232 digital converter FDC1004 available for the electronics readout. Experiments described in  
233 the following use  $t_{\text{PDMS}} = 800 \pm 50 \mu\text{m}$ .

234 The depths of the microfluidic channels are  $200 \pm 10 \mu\text{m}$ , the capping layer consists of the  
235 Mylar sheet described previously and the silicone adhesive has a thickness of  $7.6 \mu\text{m}$ . These  
236 choices yield capacitances that span the dynamic range of the FDC1004 sensor, as shown in  
237 Figure S5. The data also indicate that the increased temperature and the presence of skin  
238 underneath do not affect the results.

239 Systematic experiments using a syringe pump apparatus perfusing various liquids similar to  
240 human sweat (DI water, 50 mM NaCl, 50  $\mu\text{M}$  glucose, 15 mM lactate solutions in DI water,

241 and commercial artificial sweat) through the microfluidic channels establish a relationship  
242 between capacitance and sweat rate/loss. The studies involve filling the microfluidic channels  
243 with one of those liquids and measuring the change in capacitance as a function of the volume  
244  $V$ . Results, shown in Figure 2c, highlight that the change in capacitance is proportional to  $V$   
245 with no dependence on the composition of the liquid within physiologically relevant  
246 concentrations of electrolytes and metabolites. This measurement relies on the limited  
247 variation of the real part of the dielectric constant over the physiological range of electrolyte  
248 concentrations<sup>18</sup>, as the main parameter that affects capacitance measurements with the  
249 interdigitated array. This result allows for accurate sweat rate measurements, independent of  
250 variations in sweat composition. As a consequence, calibration results derived from Figure  
251 2c have a sensitivity of  $1.14 \text{ pF} \cdot \mu\text{L}^{-1}$ . Figure 2d shows continuous-mode measurements across  
252 multiple filling rates, controlled with a syringe pump. Figure 2d images (right panel) show  
253 different levels of sweat fill extent corresponding to three experimental points in the plot.  
254 These experiments establish the basis for on-body trials for sweat rate, without dependence  
255 on (i) detailed composition of the sweat across the physiological range, (ii) temperature, or  
256 (iii) the subjacent skin layer.

257

### 258 **Geometry optimization and benchtop testing of sweat conductivity**

259 Given that the capacitance measurements described above are independent of the  
260 composition of sweat, measurements of sweat conductivity require a dramatic change in the  
261 geometry of the channels and electrodes. The approach presented here derives from the from  
262  $C^4D$  techniques used in capillary electrophoresis.<sup>34, 35</sup> The geometry consists of two

263 microchannels with dimensions in the mm-range that connect by a narrow and long  
264 microchannel. One large electrode couples capacitively to each of the large microchannels,  
265 in a manner such that the capacitance of a pair of such electrodes exhibits a frequency  
266 spectrum that depends on the conductivity of the liquid, as detailed by Cahill et al<sup>40</sup>.  
267 Capacitance measurement using that geometry thus permits a contactless determination of  
268 liquid conductivity. Figure 3a shows an example of frequency spectra for multiple liquid  
269 conductivities (physiologically relevant for human sweat), for an optimized geometry  
270 selected according to considerations detailed below. A sharp decrease of capacitance occurs  
271 at a frequency value that increases with conductivity. Measurements at a given frequency  
272 close to that of these large variations (here 25kHz, which corresponds to FDC1004 chip  
273 operation frequency) serve as the basis for determining the conductivity. The data of  
274 Supplementary Figure S6 demonstrate that increasing the areas of the microchannels and  
275 electrodes improves the sensitivity. To avoid collapse<sup>36, 37</sup>, the geometries of these channels  
276 take the form of serpentine rather than circular shapes, as shown in Figure 1g and the inset  
277 of Figure 3b. Experiments involve layers of PDMS (800 +/- 50  $\mu\text{m}$  in thickness) with trenches  
278 (200 +/- 10  $\mu\text{m}$  in depth) covered by a capping layer of Mylar (2.5  $\mu\text{m}$  in thickness) coated  
279 with a silicone adhesive (5.4  $\mu\text{m}$  in thickness; corresponding to a spin-coating speed of 4500  
280 rpm). Figure 3b summarizes the results of FEA for the geometry (inset) used in the  
281 experiments in Figure 3a, highlighting excellent agreement with no adjustable parameters.  
282 Limiting the overall size of the device (i) improves the wearability, and (ii) provides a  
283 continuous measurement with reasonably small amount of sweat analyzed at a given time.  
284 Increasing the sizes of the large microchannels would require an excessive amount of sweat,

285 potentially more than that collected in typical exercising conditions. The geometry selected  
286 here corresponds to a volume of 12  $\mu\text{L}$  to enable the conductivity measurement. This volume  
287 is several times smaller than that collected during a representative exercising session<sup>14</sup>.  
288 FEA simulations at the operating frequency of 25 kHz provide insights into appropriate  
289 geometries, especially the dimensions of connecting channel (width,  $W_c$ ; length,  $L_c$ ) as  
290 defined in the schematic illustration of Figure 3c. Details of this 3D model, based on the  
291 electric current flow in conductive and capacitive media over a frequency domain<sup>41</sup>, are in  
292 the Materials and Methods section. The minimum value of  $W_c$  is 200  $\mu\text{m}$ , to facilitate the  
293 filling of the channel due to pressure supplied by the sweat glands<sup>33</sup>. A simplified model with  
294 two disks linked by a straight channel reveals the influence of the dimensions. Computational  
295 studies vary the parameters  $W_c$ ,  $L_c$  as well as the radius of the disks in a manner that maintains  
296 a constant total volume of 12  $\mu\text{L}$ . Details on differences between this simplified model and  
297 the actual geometry are shown in Supplementary Figure S6. Figure 3c highlights the  
298 maximum sensitivity of the capacitance to conductivity across a broad range of frequencies.  
299 Here, the sensitivity corresponds to the partial derivative of the capacitance over the  
300 dimensionless electrical conductivity at a conductivity of  $\sigma=1\text{S}\cdot\text{m}^{-1}$ . The contour plot  
301 demonstrates that a combination of small  $W_c$  and  $L_c$  provides the best sensitivity. Figure 3d  
302 shows the frequency at which the maximum sensitivity from Figure 3c occurs for various  
303 values of  $W_c$  and  $L_c$ , i.e. the frequency for which the curves in Figures 3a and 3b are most  
304 separated for different conductivities. At 25 kHz and at a conductivity of 1S/m, this  
305 simplified model suggests that the dimensions should be  $W_c = (0.2 - 0.3)$  mm and  $L_c = (5 -$   
306 6 mm) to maximize the sensitivity.



307 Figure 3e provides experimental results on geometry optimization, using  $W_c=0.2$  mm for  
308 various pad areas,  $p$ , defined as the area of each set of serpentine channel, and channel length  
309  $L_c$ . Experiments confirm that increasing the sizes of the pads increases the capacitance,  
310 consistent with numerical results in Supplementary Figure S6. Results also demonstrate that  
311 the case of  $p=27$  mm<sup>2</sup> and  $L_c=3$  mm exhibits a linear relationship between the change in  
312 capacitance (at 25 kHz) with the largest slope over the entire range of conductivity. As  
313 suggested previously, the measured capacitances span a significant fraction of the operating  
314 range of the FDC1004 chip. Further experiments (including on-body testing), as well as  
315 examples shown in Figure 3a and 3b exploit this optimized geometry.

316 The millimeter-scale electrodes and spacings for this conductivity system lead to a high level  
317 of sensitivity to the skin underneath. For that reason, the device design includes a shielding  
318 copper plane between the measurement system and the skin. The full stack of materials  
319 appears above and in Figure 1g. The results of Figure 3f demonstrate that this shielding leads  
320 to behaviors that are similar on skin and in air. In both cases, the change in capacitance for  
321 filled and empty channels depends linearly on the conductivity of the liquid. The experiments  
322 shown in Figure 3a, e, and f involve multiple NaCl solutions and an artificial sweat solution  
323 ( $0.893$  S.m<sup>-1</sup>). These results establish a calibration curve that can be used for on-body trials,  
324 with a sensitivity on skin of  $13.9$  pF (S.m<sup>-1</sup>)<sup>-1</sup>.

325

### 326 **Digital signals and readout design**

327 Wireless digital analysis of sweat rate and conductivity, in real-time, is critically important  
328 for practical applications of this technology. Rapid prototyping techniques form flexible

329 electronics boards of polyimide and copper, on which components can be soldered to yield a  
330 functional electronics system for capacitive readout and wireless Bluetooth transmission  
331 capabilities. The design includes the following electronics subsystems: (i) a capacitance-to-  
332 digital converter (FDC 1004, Texas Instruments) that supports a measurement range of +/-  
333 15pF around an offset that can be set between 0 and 100 pF, (ii) a microcontroller (nFR52832,  
334 Nordic Semiconductor) that captures data from the capacitance-to-digital converter and  
335 transmits information wirelessly and, (iii) a Li-Polymer battery (12 to 45mAh) that provides  
336 power to the system. A software routine on a tablet serves as a user-friendly interface to  
337 connect to the sensors, start/stop the acquisition process and set the parameters to control the  
338 measurement range and sampling frequency. The overall operating scheme is in Figure 4a  
339 and electronics schematics are in Supplementary Figure S7. Encapsulating the electronics in  
340 a low modulus silicone elastomer provides a safe and soft interface to the skin. Bluetooth  
341 transmission allows robust data collection, with no dropouts observed within a 5 m distance  
342 between the device and a Bluetooth dongle connected to the tablet.

343

#### 344 **On-body field trials during physical exercise**

345 Intimate skin coupling requires wearable devices that can bend and conform to curvilinear  
346 surface of the human body. Data presented in Supplementary Information Figure S8 show  
347 that the geometry and choice of materials allow bending (but not stretching) to a degree that  
348 allows accurate measurements in typical mounting locations on the body. Human subject  
349 testing involves evaluations on healthy young adult volunteers during exercise on stationary  
350 bikes. Detailed protocols are in the Materials and Methods section. Devices attach to the skin

351 on the forehead and capacitance data passes wirelessly, in real time, to a tablet (Figure 4a).  
352 Images captured at defined time intervals allow for secondary measurements of the filling  
353 front with a dye to facilitate visibility of the sweat. Measurements of sweat conductivity rely  
354 on small samples pipetted from the device during exercising (for droplets at the outlet) and  
355 at the end of the exercising session (for liquid left inside the channel). Dilution followed by  
356 measurements with a conductivity meter yields an average conductivity for the trial, as  
357 another comparative measure. All measurements of capacitance ( $\Delta C$ ) correspond to the  
358 difference between the capacitance at a particular time and that captured before the start of  
359 the exercising session.

360 Figure 4b shows on-body results of sweat rate compared to the benchtop calibration obtained  
361 in Figure 2c, indicating strong agreement between bench and on-body results. Inset of Figure  
362 4b shows the temporal evolution of measured volume for all subjects, highlighting that the  
363 benchtop calibration holds for both low (red crosses) and high (purple diamonds) sweat rates.  
364 The volume indicated in abscissa corresponds to the actual volume minus 3.4  $\mu\text{L}$  of dead  
365 volume near the inlet, where it interacts with the blue dye. This dead volume space can be  
366 reduced in devices that do not require the dye. For one subject (represented with orange  
367 triangles), a small delamination of the electrodes likely occurred during sweat flow, causing  
368 a reduction in the value of  $\Delta C$ .

369 Figure 4c shows on-body measurements of sweat conductivity. The capacitance increases  
370 slightly (by  $\sim 0.5$  pF) as the sweat fills the first pad. Upon filling of the second pad, the  
371 capacitance rises to a large value, and recording of the electrolyte content becomes possible.  
372 Data in Figure 4c correspond to the difference between the baseline and the average of the

373 recorded data once the device is filled and continuously collects more recent sweat, as  
374 illustrated in the inset. Standard laboratory procedures involve measurements of conductivity  
375 of an entire sample of sweat, as a single averaged value. Such an evaluation provides a certain  
376 level of validation but fails to capture the full temporal evolution. Figure 4c shows that the  
377 calibration curve observed on skin with solutions of various conductivities in Figure 3f is in  
378 good agreement with averaged data recorded during exercise. This measurement is also  
379 sensitive to the temperature inside the channels, as the conductivity varies with temperature.  
380 A detailed discussion on the effect of temperature on the results for benchtop experiments in  
381 controlled conditions is in Figure S9. As an additional point, observed changes in capacitance  
382 over time, which manifest often as a decrease in our trials, suggest that the conductivity of  
383 the sweat decreases during this period. The limited number of trials in this study coupled to  
384 the effects of possible residual ions on the skin or of temperature variations prevent firm  
385 conclusions. Further investigations of these trends are necessary, especially as some recent  
386 studies report strong variations from person to person for temporal variations of ionic charge  
387 during exercising<sup>17</sup>. Details on the experimental protocol for on-body trials are in the  
388 Materials and Methods section.

389

## 390 **Conclusions**

391 The flexible, skin-mounted platforms presented here illustrate an important, non-contact  
392 approach in interfacing electronics modules and capacitance-based electrodes with  
393 microfluidic systems for sweat collection. Electrodes coupled capacitively to single-use  
394 microfluidics are capable of real-time measurements of sweat rate and sweat conductivity

395 during physical exercise. Optimized channel and electrode designs, together with an ultrathin  
396 capping layer, enable reliable and accurate measurements from a lightweight, conformal  
397 platform that can mount on most regions of the body. A magnetic coupling scheme allows  
398 for repeated use of an electronics module that digitizes and transmits capacitive  
399 measurements to a tablet. Field trials establish the practical utility of the technology for use  
400 in fitness and sports with potential utility in other contexts, including medical monitoring and  
401 diagnostics.

402

### 403 **Materials and methods**

404 *Fabrication of flexible and reusable electrode platforms:* Preparation starts with the  
405 fabrication of a chromium (Cr) photomask, exposed with a maskless aligner (30 mJ.cm<sup>-2</sup>;  
406 MLA150; Heidelberg Instruments), developed in 1:4 mixture of developer AZ400k  
407 (Microchemicals) and DI water, rinsed with DI water, etched with Cr etchant (CEP-200  
408 chromium etchant; Microchrome Technology Products), and subsequently cleaned with DI  
409 water, acetone and isopropanol. To form the electrodes, polydimethylsiloxane (20:1  
410 base:curing agent weight ratio, Sylgard 184, Dow Corning) spin-coated at 1500 rpm for 30s  
411 onto a glass slide (Fisherbrand) yielded a sticky layer as a support for lamination of a flexible  
412 polyimide (PI, 25 μm)-copper (Cu, 9 μm) clad foil (Pyr lux AC092500EV; DuPont). Curing  
413 at 70°C for 3 h created strong bonds between the support and the clad sheet, with Cu facing  
414 up. Standard photolithography techniques then patterned the Cu: after spinning a layer of  
415 photoresist (AZ4620P; Microchemicals) at 3000 rpm for 30 s and baking on a hotplate at  
416 110 °C for 2 min, exposure with ultraviolet (UV) light (10 mJ cm<sup>-2</sup>) through our photomask,

417 developing (in 1:4 mixture of developer AZ400k; Microchemicals) and rinsing with DI water  
418 formed patterns of photoresist. Cu wet etching (HFCE100 copper etchant; Transene), DI  
419 water rinsing, and subsequent resist removal by rinsing with acetone and isopropanol yielded  
420 a PI-Cu foil with electrodes in desired geometries. Upon release from the glass slide,  
421 deposition of a 1  $\mu\text{m}$  conformal coating of parylene-C provided a protective layer on the  
422 entire sample, excluding connection pads protected with Kapton tape during deposition (SCS  
423 Labcoater 2 Parylene system, Specialty Coating Systems). Figure S10a summarizes this  
424 process.

425

426 *Fabrication of an ultra-thin capping layer for the microfluidics channels:* Microfluidic  
427 channels were formed using soft lithography techniques. More precisely, spin coating KMPR  
428 1010 (Microchem) at 3000 rpm for 30 s formed a 15  $\mu\text{m}$  thick layer of photoresist on a 1mm-  
429 thick, 4 inch silicon wafer. Baking at 100°C on a hotplate for 3 min, exposing to UV light  
430 (10  $\text{mJ}\cdot\text{cm}^{-2}$ ) through a photomask (fabricated using similar technique as for the previously  
431 described photomask), post-baking for 2 min at 110°C, immersing in developer (AZ 917 MIF;  
432 Integrated Micro Materials) and rinsing with DI water yielded a wafer with patterned  
433 photoresist. Deep reactive ion etching (STS Pegasus ICP-DRIE, SPTS Technologies Ltd)  
434 then created trenches to depths of 200 +/-10  $\mu\text{m}$  on the surface of the wafer. Pouring liquid  
435 PDMS (10:1 base:curing agent, Sylgard 184, Dow Corning) on the mold, spin coating at 100  
436 rpm and curing at 120°C on a hotplate formed the channel layer (thickness 800+/-50  $\mu\text{m}$ ).  
437 Figure S10b summarizes this procedure. For channels designed for measurements of sweat  
438 rate, a 1.5 mm diameter circular punch (Reusable biopsy punch, World Precision Instruments)

439 formed holes at the inlet of the channel layer. A Mylar film with thickness of 2.5  $\mu\text{m}$   
440 (Spectromembrane, Chemplex) served as a capping layer. After treating in a UVO-cleaner  
441 for 4 min, immersing in a solution of (3-Aminopropyl)triethoxysilane (Sigma-Aldrich) in DI  
442 water at a 1:50 volume ratio for at least 1 h, and rinsing with DI water, lamination of the  
443 Mylar film on a sacrificial soft elastomer layer (Ecoflex 30, Smooth-On) yielded a platform  
444 to facilitate assembly with PDMS channels. After a 4-min UVO-treatment, laminating the  
445 PDMS channels onto the Mylar sealed the channels. Release from the Ecoflex layer and  
446 baking overnight at 70°C in an oven yielded strongly bonded microchannels with an ultra-  
447 thin capping layer, as illustrated in Figure S1a.

448 For channels designed to measure sweat conductivity, a 1.5 mm diameter hole formed in the  
449 Mylar allowed sweat to enter the channels. Assembly of the layer containing the channels  
450 (PDMS trenches and Mylar capping layer) onto a flat 800 $\pm$ 50  $\mu\text{m}$  PDMS layer with a 1.5  
451 mm hole aligned with that of the Mylar, relied on a JMS#903 adhesive (Label Innovation)  
452 around the inlet zone. This process yielded a device that allowed insertion and removal of  
453 the electrodes and the shield plane in between the bottom PDMS layer and the Mylar layer,  
454 as shown in Figure 1g.

455 In both systems, the Mylar served as a foundation for repositionable adhesives (MG1010  
456 adhesive, Dow Corning) spin-coated at 3500 rpm for the sweat rate channel and at 4500 rpm  
457 for the sweat conductivity channel for 5 min resulted in a thin (7.6  $\mu\text{m}$  or 5.4  $\mu\text{m}$ ) coatings.  
458 After drying for 5 min at 70°C and cooling down to room temperature, bleached Kraft paper  
459 with silicone release (3M) laminated onto the adhesive coating protected it from dust and  
460 damage.

461

462 *Analytical model for optimizing sweat rate sensor:*

463 A 2-D analytical model determined the optimal number of electrodes and the thickness of the  
 464 dielectric (capping) layer. Due to symmetry and periodicity<sup>39</sup>, the total capacitance can be  
 465 written as

$$466 \quad C \approx (N - 1) \frac{C_I}{2} \quad (1)$$

467 where  $N$  is the number of electrodes in the system, and  $C_I$  is the half capacitance of one  
 468 interior electrode with respect to the ground plane as shown in Figure S11a.

469 For a half plane space consisting of two layers as in Figure 2a, the capacitance  $C_I$  is a  
 470 function of two non-dimensional geometric parameters  $\eta$  and  $\frac{t}{\lambda}$ . The solution of  $C_I$  is  
 471 obtained with conformal mapping techniques, and the contributions from different layers are  
 472 summed up in a parallel scheme ( $\epsilon_1 < \epsilon_2$ ) or serial scheme ( $\epsilon_1 > \epsilon_2$ ) as shown in Figure S11b.  
 473 The complete derivation of  $C_I$  and  $C_E$  can be found in the analytical model<sup>35</sup>.

474

475 *FEA simulations for optimizing sweat conductivity sensor:*

476 3-D finite element analysis was performed using commercial FEA software (COMSOL) to  
 477 determine the frequency dependent capacitive behavior for fluid conductivities and to  
 478 optimize the connecting channel length for maximum sensitivity<sup>41</sup>. Voltage applied at  
 479 electrodes and a corresponding current response gives the complex impedance  $Z^*$ . The  
 480 equivalent capacitance  $C$  is then determined as

$$481 \quad C = \text{Im}\left(\frac{1}{\omega Z^*}\right) \quad (3)$$



482 and the sensitivity is defined as the partial derivative of the capacitance over the electrical  
483 conductivity  $\partial C/\partial\sigma$ . The electrode pads, microchannels, fluid, and material layers are  
484 modeled using 4-node tetrahedral elements. To account for the Parylene-C/adhesive/mylar  
485 multilayer structure, we consider a homogeneous dielectric layer of 9  $\mu\text{m}$  thickness.  
486 Convergence test of the mesh size had been performed to ensure accuracy. The total  
487 number of elements in the models is approximately  $\sim 910,000$ . A parameters table is  
488 provided in Supplementary Information Figure S12.

489

490 *Preparation of standard test solutions:* Mixing NaCl (certified ACS; Fisher Chemicals), D  
491 (+) glucose or (L+) lactic acid (Sigma-Aldrich) in DI water yielded single-analyte solutions  
492 with physiologically relevant sodium chloride (NaCl, 25 to 100 mM)<sup>42</sup>, glucose (50  $\mu\text{M}$ )<sup>14,33</sup>  
493 and lactate (15 mM)<sup>43</sup> concentrations. An artificial sweat solution containing several  
494 electrolytes, minerals, metabolites and amino acids (stabilized artificial eccrine perspiration  
495 1700 – 0020; Pickering Laboratories) and DI water (HPLC grade; Fisher chemicals) served  
496 as additional test solutions. Probing the DI water, NaCl and artificial sweat solutions with a  
497 conductivity meter (SevenMulti, Mettler Toledo) yielded their conductivities.

498

499 *Benchtop testing of devices with an impedance analyzer:* An impedance analyzer (E4990A;  
500 Keysight Technologies) served as a system for quantifying the sensor capacitance. Inserting  
501 polytetrafluorethylene tubing (PTFE; Cole-Parmer Instrument Company) and sealing the  
502 microchannel inlet with epoxy facilitated the introduction of a test fluid using a syringe. For  
503 consecutive tests with solutions of various conductivities, injection of fluids in an order of

504 increasing conductivity with separate syringes minimized the effect of contamination.  
505 Characterization at room temperature involved connecting the electrodes via alligator clips  
506 to the measurement instrument and suspending the assembled device at least 3 cm above the  
507 work surface to minimize parasitic capacitances during measurements. Performing a  
508 frequency sweep from 1 kHz to 10 MHz then yielded the capacitance spectra.

509

510 *Fabrication of wireless readout electronics:* Designing the electronics layout with e-CAD  
511 software and cutting with a LPKF Protolaser U4 yielded a double-sided flexible electronics  
512 board cut in a 75  $\mu\text{m}$  Cu / 18  $\mu\text{m}$  PI / 75  $\mu\text{m}$  Cu sheet (Pyrulux, DuPont). Soldering of the  
513 following components then yielded a functional electronics readout platform (once connected  
514 magnetically to a Li-Polymer battery (12mAh to 45mAh)): nRF52832 (Nordics  
515 Semiconductor) Bluetooth Low Energy chip, 2.4Ghz ceramic antenna (Johanson  
516 Technology), ISL9016 (Renesas Electronics) LDO to reduce operating voltage to 3.3V,  
517 FDC1004 (Texas Instruments) capacitance-to-digital converter, as well as multiple passive  
518 components (402 and 201 sizes). High temperature neodymium magnets soldered to the  
519 board facilitated reversible connectivity between the modules: four 0.04'' thick 0.1''  
520 diameter magnets (McMaster) for connection to the electrodes and shield, and two 0.06''  
521 thick 1/8'' diameter magnets (McMaster) for connection to the battery. Magnets of opposite  
522 polarity soldered on the electrodes and on the battery allowed for a secure connection, with  
523 an alternation in the orientations of the magnets so that only one mounting position is possible.  
524 The flexible board and the battery were then encapsulated in thin low modulus silicone shell  
525 (Silbione 4420 RTV, Elkem Silicones, mixed with Silc-Pig silicone dye, Smooth-On) to yield

526 in a soft platform without exposed electronic components or wiring. Validation of the  
527 performance of the electronics was performed using capacitors of known values.  
528 Measurements on the electronics readout part (C) with a power profile system show that the  
529 average current is 780  $\mu\text{A}$  when connected to the BLE host at the operating frequency, which  
530 allows to run multiple exercising sessions with one charged battery.

531

532 *In situ measurements of sweat rate and conductivity from human trials:* Testing involved  
533 healthy young adult volunteers, cycling at moderate to high intensity at ambient temperature  
534 and humidity conditions. Prior to the trial, skin-safe adhesive (1524, 3M) cut to appropriate  
535 shapes (board outline and a 6mm diameter hole at the inlet to allow sweat to enter the device)  
536 and treated on one side with a UVO-cleaner (to allow secure bonding to the device) provided  
537 an easy-to-peel adhesive interface to the skin. Before attachment of the device, cleaning of  
538 skin by rubbing with an isopropyl alcohol prep pad (Dynarex) limited contamination of new  
539 sweat samples with residual ions present on the skin. Microfluidics and electrodes patches  
540 laminated on skin coupled through magnets to the electronic readout unit, which transmitted  
541 data to the tablet (Surface Pro, Microsoft) through a Bluetooth dongle (Nordics  
542 Semiconductor nRF52 development kit), placed at a distance between 2 and 5 m from the  
543 subject, with a sampling frequency of 0.1 Hz, which is sufficient to capture variations over  
544 physiologically relevant timescales. The ability of the sensors to detect rapid changes in flow  
545 rate and conductivity depend mainly on their geometry. For sweat rate measurements, the  
546 characteristic dimensions of the interdigitated electrodes allow assessments of fluid  
547 progression in the channel at appropriate scales. For sweat conductivity, the sensor must fill

548 with sweat (at least 12  $\mu\text{L}$ ) for an initial measurement, with a continuous capability thereafter,  
549 as sweat in the sensor is progressively replaced. Data collection included sweat rate and/or  
550 conductivity from one or two patches placed on the forehead, on one or two tablets. Mounting  
551 on the forehead corresponds to a case for which wireless transmission of data to a tablet is  
552 especially relevant, as visual inspection cannot be performed easily by the individual wearing  
553 the device. In addition, the relatively high sweat rates that occur at that location facilitate  
554 validation of the device during medium intensity exercising sessions by ensuring a complete  
555 filling of the channels. The microfluidic structures were used only once. The electrodes and  
556 electronics were sanitized and reused. Photographs of the sweat rate device captured at  
557 random time intervals during each exercising session allowed comparison to reference data  
558 for sweat rate, with blue dye to enhance visibility (Americolor Soft Gel Paste, Blue).  
559 Measurements of conductivity of diluted sweat were performed with a laboratory bench  
560 conductivity meter (SevenCompact S230 with InLab751 4 mm probe, Mettler Toledo) as  
561 reference data for sweat conductivity. For the conductivity measurement system, sweat  
562 collected from the channels with a micropipette contained no dye to avoid any potential  
563 contamination issues, and conductivity measurements at two temperatures were linearly  
564 extrapolated to a temperature of 22°C, corresponding to the temperature at which benchtop  
565 validation was performed.

566

### 567 **Acknowledgements**

568 This work utilized Northwestern University Micro/Nano Fabrication Facility (NUFAB),  
569 which is partially supported by Soft and Hybrid Nanotechnology Experimental (SHyNE)

570 Resource (NSF ECCS-1542205), the Materials Research Science and Engineering Center  
571 (DMR-1720139), the State of Illinois, and Northwestern University. The work was supported  
572 by the Querrey-Simpson Institute for Bioelectronics at Northwestern University. R.G., T.R.R.  
573 and A.J.A. acknowledge support from the National Institute on Aging of the National  
574 Institutes of Health (NIH R43AG067835). R.A. acknowledges support from the National  
575 Science Foundation Graduate Research Fellowship (NSF grant number 1842165) and Ford  
576 Foundation Predoctoral Fellowship. We thank 3M, Inc. for providing access to the 1524  
577 adhesive used in this work.

578

#### 579 **Conflicts of interest**

580 J.A.R., W.L., S.P.L., J.B.M., A.J.A., and R.G. are co-founders and/or employees of a  
581 company, Epicore Biosystems, Inc., which develops soft microfluidics systems for  
582 commercial deployment.

583

#### 584 **Authors contributions**

585 A.H.-F., S.S., Y.X., R.A., Y.G., R.G., Y.H. and J.A.R. conceived the project, led overall  
586 development of concepts, organization of system, designed a combination of experimental  
587 and modeling work and interpreted results. A.H.-F., S.S., and Y.G. led bench top  
588 experimental work on microfluidics channels and electrodes, with support from S.K., P.G.,  
589 J.C., T.R.R., A.J.A and R.G. through fruitful discussions and help for samples fabrication.  
590 Y.X., R.A. and Y.H. designed and performed all theoretical and simulation modeling of the  
591 systems, providing guidelines for experimental work. A.H.-F., S.S., Y.G., and C.L. prepared

592 designs for microfluidics and electrodes integration in a wearable format, with assistance  
593 from K.B.F. and B.V.P. for fabrication and from M.S.R., A.J.B., A.J.A., W.L., and R.G. for  
594 fruitful discussions. M.S.R., A.H.-F., and S.S. designed electronics readout system with  
595 support from B.V.P., K.H.L., H.U.C., W.L., S.P.L., J.B.M, and A.J.A. Also, W.L. led  
596 software development with support from J.-Y.L., S.P.L., J.B.M. and A.J.A. Finally, A.H.-F.,  
597 C.L., K.B.F., B.V.P., K.H.L., M.J., A.J.B. worked on on-body trials of wearable devices.  
598 A.H.-F, S.S., Y.X., R.A., T.R.R., R.G., Y.H. and J.A.R led the article draft writing and all  
599 authors proofread the manuscript.

600

601 **References**

- 602 1. K. Sato, *Reviews of Physiology, Biochemistry and Pharmacology*, 1977, **79**, 51--  
603 131.
- 604 2. P. M. Farrell, B. J. Rosenstein, T. B. White, F. J. Accurso, C. Castellani, G. R.  
605 Cutting, P. R. Durie, V. A. LeGrys, J. Massie, R. B. Parad and others, *The Journal of*  
606 *pediatrics*, 2008, **153**, S4--S14.
- 607 3. Z. Sonner, E. Wilder, J. Heikenfeld, G. Kasting, F. Beyette, D. Swaile, F. Sherman,  
608 J. Joyce, J. Hagen, N. Kelley-Loughnane and others, *Biomicrofluidics*, 2015, **9**, 031301.
- 609 4. L. B. Baker, K. A. Barnes, M. L. Anderson, D. H. Passe and J. R. Stofan, *Journal*  
610 *of sports sciences*, 2016, **34**, 358--368.
- 611 5. R. J. Maughan and S. M. Shirreffs, *International journal of sport nutrition and*  
612 *exercise metabolism*, 2008, **18**, 457--472.
- 613 6. J. Choi, R. Ghaffari, L. B. Baker and J. A. Rogers, *Science Advances*, 2018, **4**.

- 614 7. A. Koh, D. Kang, Y. Xue, S. Lee, R. M. Pielak, J. Kim, T. Hwang, S. Min, A.  
615 Banks, P. Bastien, M. C. Manco, L. Wang, K. R. Ammann, K.-I. Jang, P. Won, S. Han, R.  
616 Ghaffari, U. Paik, M. J. Slepian, G. Balooch, Y. Huang and J. A. Rogers, *Science*  
617 *Translational Medicine*, 2016, **8**, 366ra165--366ra165.
- 618 8. Y. Sekine, S. B. Kim, Y. Zhang, A. J. Bandodkar, S. Xu, J. Choi, M. Irie, T. R.  
619 Ray, P. Kohli, N. Kozai, T. Sugita, Y. Wu, K. Lee, K.-T. Lee, R. Ghaffari and J. A. Rogers,  
620 *Lab Chip*, 2018, **18**, 2178-2186.
- 621 9. A. J. Bandodkar, D. Molinnus, O. Mirza, T. Guinovart, J. R. Windmiller, G.  
622 Valdés-Ramírez, F. J. Andrade, M. J. Schöning and J. Wang, *Biosensors and*  
623 *Bioelectronics*, 2014, **54**, 603 - 609.
- 624 10. S. B. Kim, K. Lee, M. S. Raj, B. Lee, J. T. Reeder, J. Koo, A. Hourlier-Fargette, A.  
625 J. Bandodkar, S. M. Won, Y. Sekine, J. Choi, Y. Zhang, J. Yoon, B. H. Kim, Y. Yun, S.  
626 Lee, J. Shin, J. Kim, R. Ghaffari and J.A. Roger, *Small*, 2018, **14**, 1802876.
- 627 11. J. T. Reeder, J. Choi, Y. Xue, P. Gutruf, J. Hanson, M. Liu, T. Ray, A. J.  
628 Bandodkar, R. Avila, W. Xia, S. Krishnan, S. Xu, K. Barnes, M. Pahnke, R. Ghaffari, Y.  
629 Huang and J. A. Rogers, *Science Advances*, 2019, **5**.
- 630 12. J. L. Lezana, M. H. Vargas, J. Karam-Bechara, R. S. Aldana and M. E. Furuya,  
631 *Journal of Cystic Fibrosis*, 2003, **2**, 1--7.
- 632 13. H. Emrich, E. Stoll, B. Friolet, J. Colombo, R. Richterich and E. Rossi, *Pediatric*  
633 *research*, 1968, **2**, 464.

- 634 14. J. Choi, A. J. Bandonkar, J. T. Reeder, T. R. Ray, A. Turnquist, S. B. Kim, N.  
635 Nyberg, A. Hourlier-Fargette, J. B. Model, A. J. Aranyosi, S. Xu, R. Ghaffari and J. A.  
636 Rogers, *ACS Sensors*, 2019, **4**, 379-388.
- 637 15. J. Francis, I. Stamper, J. Heikenfeld and E. F. Gomez, *Lab Chip*, 2019, **19**, 178-  
638 185.
- 639 16. H. Y. Y. Nyein, L. Tai, Q. P. Ngo, M. Chao, G. B. Zhang, W. Gao, M. Bariya, J.  
640 Bullock, H. Kim, H. M. Fahad and A. Javey, *ACS Sensors*, 2018, **3**, 944--952.
- 641 17. Z. Yuan, L. Hou, M. Bariya, H. Y. Y. Nyein, L. Tai, W. Ji, L. Li and A. Javey, *Lab*  
642 *on a Chip*, 2019, **19**, 3179--3189.
- 643 18. J. B. Hasted, D. M. Ritson and C. H. Collie, *The Journal of Chemical Physics*,  
644 1948, **16**, 1-21.
- 645 19. A. N. Romanov, *Biophysics*, 2010, **55**, 473--476.
- 646 20. C. Elbuken, T. Glawdel, D. Chan and C. L. Ren, *Sensors and Actuators A:*  
647 *Physical*, 2011, **171**, 55 - 62.
- 648 21. P. K. Isgor, M. Marcali, M. Keser and C. Elbuken, *Sensors and Actuators B:*  
649 *Chemical*, 2015, **210**, 669 -- 675.
- 650 22. L. L. Sohn, O. A. Saleh, G. R. Facer, A. J. Beavis, R. S. Allan and D. A.  
651 Notterman, *Proceedings of the National Academy of Sciences*, 2000, **97**, 10687--10690.
- 652 23. S. Emaminejad, M. Javanmard, R. W. Dutton and R. W. Davis, *Lab on a Chip*,  
653 2012, **12**, 4499 -- 4507.
- 654 24. Y. Temiz and E. Delamarche, *Scientific Reports*, 2018, **8**, 10603.



- 655 25. M. N. M. Nawi, A. A. Manaf, M. F. A. Rahman, M. R. Arshad and O. Sidek, *IEEE*  
656 *Sensors Journal*, 2015, **15**, 1738--1746.
- 657 26. J. Z. Chen, A. A. Darhuber, S. M. Troian and S. Wagner, *Lab Chip*, 2004, **4**, 473-  
658 480.
- 659 27. M. Vakilian and B. Y. Majlis, presented in part at the Semiconductor electronics  
660 (ICSE), 2014 IEEE international conference on, 2014.
- 661 28. J. W. Kim, P. Pasupathy, S. Zhang and D. P. Neikirk, presented in part at the  
662 Sensors, 2009 IEEE, 2009.
- 663 29. M. Demori, V. Ferrari, P. Poesio and D. Strazza, *Sensors and Actuators A:*  
664 *Physical*, 2011, **172**, 212 - 219.
- 665 30. A. J. R. Hillier, V. Makarovaite, C. W. Gourlay, S. J. Holder and J. C. Batchelor,  
666 *IEEE Sensors Journal*, 2019, DOI: 10.1109/JSEN.2019.2909353, 1-1.
- 667 31. X. Huang, W.-H. Yeo, Y. Liu and J. A. Rogers, *Biointerphases*, 2012, **7**, 52.
- 668 32. X. Huang, Y. Liu, H. Cheng, W.-J. Shin, J. A. Fan, Z. Liu, C.-J. Lu, G.-W. Kong,  
669 K. Chen, D. Patnaik and others, *Advanced Functional Materials*, 2014, **24**, 3846--3854.
- 670 33. J. Choi, Y. Xue, W. Xia, T.R. Ray, J. T. Reeder, A. J. Bandodkar, D. Kang, S. Xu,  
671 Y. Huang and J. A. Rogers, *Lab on a Chip*, 2017, **17**, 2572--2580.
- 672 34. A. J. Zemmann, *Electrophoresis*, 2003, **24**, 2125--2137.
- 673 35. P. Kubáň and P. C. Hauser, *Lab on a Chip*, 2005, **5**, 407--415.
- 674 36. Y. Xue, D. Kang, Y. Ma, X. Feng, J. A. Rogers and Y. Huang, *Extreme Mechanics*  
675 *Letters*, 2017, **11**, 18 - 23.

- 676 37. X. Wang, S. Chen, Y. Zhang, L. Li, Y. Xue, H. Luan and Y. Ma, *Applied Physics*  
677 *Letters*, 2018, **113**, 163702.
- 678 38. V. Sunkara, D.-K. Park, H. Hwang, R. Chantiwas, S. A. Soper and Y.-K. Cho, *Lab*  
679 *on a Chip*, 2011, **11**, 962--965.
- 680 39. R. Igreja and C. J. Dias, *Sensors Actuators, A: Physical*. 2004, **112**, 291–301.
- 681 40. B.P. Cahill, R. Land, T. Nacke, M. Min and D. Beckmann, *Sensors and Actuators*  
682 *B: Chemical*, 2011, **159**, 286-293
- 683 41. COMSOL Multiphysics. AC/DC Module User's Guide, v. 5.2. COMSOL AB,  
684 Stockholm, Sweden. 2016.
- 685 42. S. M. Shirreffs and R.J. Maughan, *Journal of Applied Physiology*, 1997, **82**, 336--  
686 341.
- 687 43. C. J. Harvey, R. F. LeBouf and A. B. Stefaniak, *Toxicology in Vitro*, 2010, **24**,  
688 1790--1796.
- 689

Figures

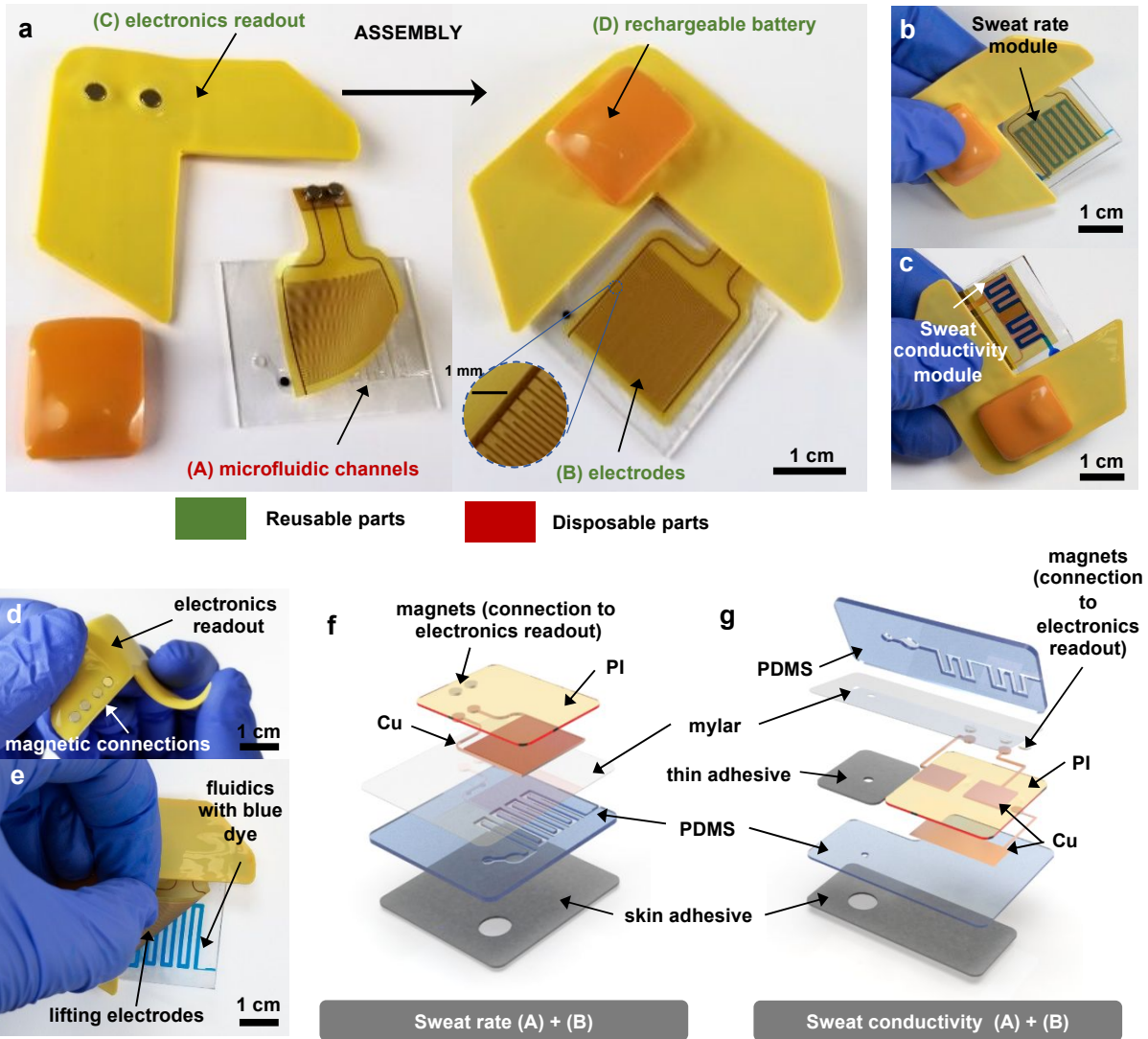


**Figure 1. Pictures and schematic illustrations of a wireless microfluidics and electronics device with capabilities in digital measurements of sweat loss, sweat rate and sweat conductivity.**

- a. General overview of device assembly, showing disposable (A) and reusable (B, C, D) parts: microfluidics channels (A) are assembled to electrodes (B) through a thin silicone adhesive coating. Electrodes connection to electronics readout (C) ensured through magnets allows

wirelessly transmission of data, using battery (D) as a powering source, connected through magnets to (C).

- b. Fully assembled device for sweat rate measurements, with blue dyed liquid in the microfluidic channel to aid visualization.
- c. Fully assembled device for sweat conductivity measurements, with blue dyed liquid in the microfluidic channel to aid visualization.
- d. Bending of the electronics readout part, showing high flexibility and low profile.
- e. Peeling of reusable electrodes from the microfluidics module, illustrating reusability of parts (B, C, D).
- f. Exploded view schematic illustrations of parts (A) and (B) for the sweat rate device.
- g. Exploded view schematic illustrations of parts (A) and (B) for the sweat conductivity device.

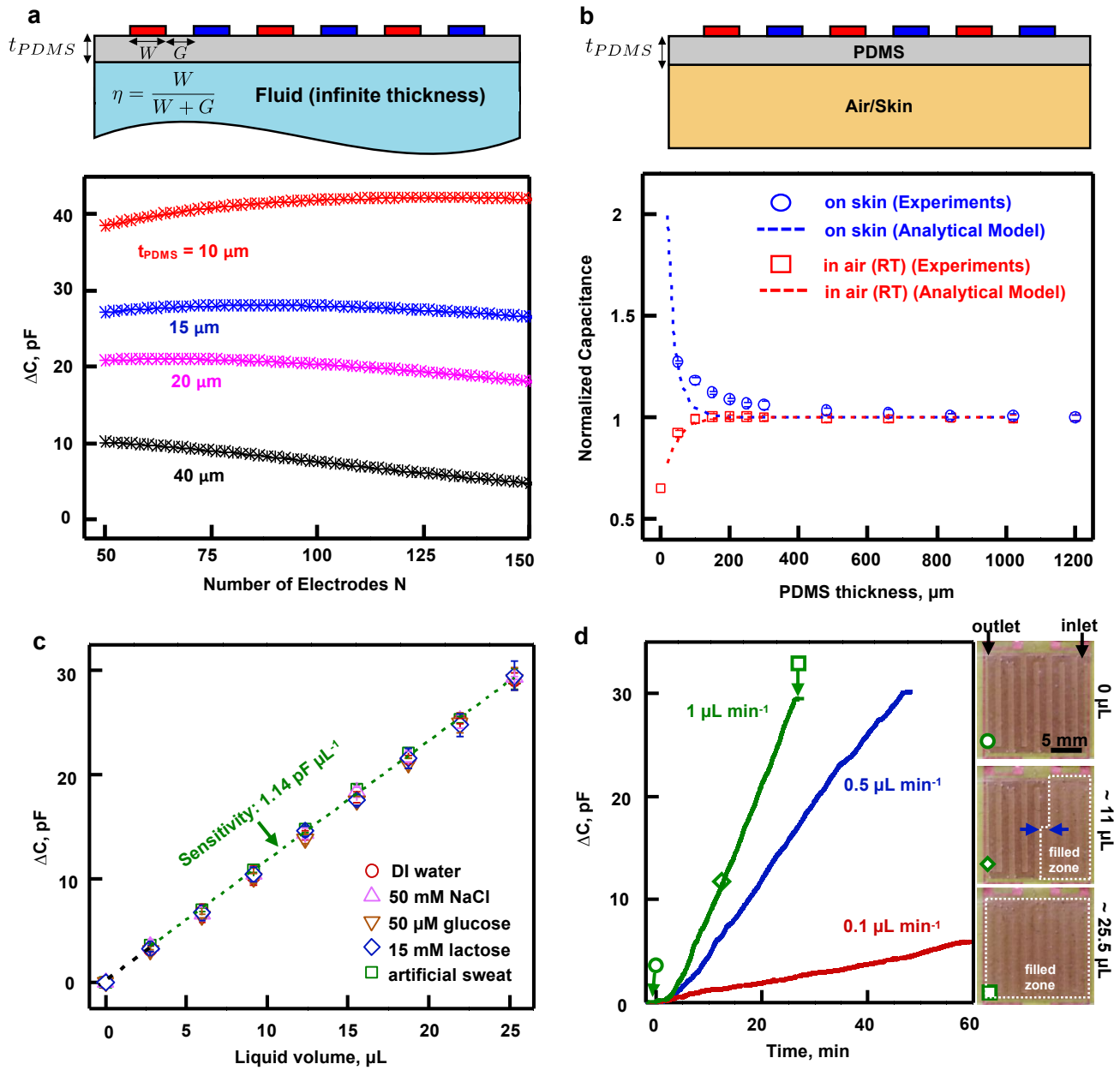


**Figure 2. Geometry optimization and benchtop evaluation of sweat rate channels and electrodes.**

- a. An interdigitated array of electrodes with width  $W$  and spacing  $G$  covers an infinite area filled either by air or liquid, with a thickness  $t_{PDMS}$  ( $\eta=0.375$ , area  $1.5\text{ cm} \times 1.5\text{ cm}$ ). The graph shows analytical simulation results of the capacitance difference for the bottom half

- space between two situations: filled with water and filled with air, as a function of the number of electrodes, for a constant area, for multiple  $t_{\text{PDMS}}$ .
- b. A bulk piece of PDMS of thickness  $t_{\text{PDMS}}$  separates an interdigitated electrodes array of dimensions  $W=75\mu\text{m}$ ,  $G=125\mu\text{m}$ , covering an area  $1.5\text{ cm} \times 1.5\text{ cm}$ , from a material under test which is either air or skin. The graph shows the capacitance measured experimentally with an impedance analyzer at 25 kHz (open symbols) and analytical simulations (dashed lines) for air (in red) and skin (in blue), normalized by the capacitance values at large thicknesses of PDMS ( $\eta=0.375$ ,  $L=1.5\text{ cm}$ ,  $\lambda=400\text{ }\mu\text{m}$ ,  $N=76$ ). The results provide guidelines for insulation of the device from the skin by a layer of PDMS.
  - c. Capacitance change (between empty and filled channel) measured with the FDC1004 chip as a function of liquid volume in the channels for DI water (red circles), 50 mM NaCl (purple upwards pointed triangles), 50  $\mu\text{M}$  glucose (brown downwards pointed triangles), 15 mM lactate (blue diamonds) and artificial sweat solution (green squares) at room temperature in air. All liquids show the same linear relation between capacitance change and volume. The results confirm the robustness of the sweat rate measurement, independent of sweat composition. Sensitivity is  $1.14\text{ pF} \cdot \mu\text{L}^{-1}$ . Error bars correspond to measurements on 3 different samples.
  - d. Continuous, real-time capacitance change recorded with the FDC1004 chip when artificial sweat flows into the microchannels at rates of 0.1 (pink), 0.5 (blue) and  $1\text{ }\mu\text{L}\cdot\text{min}^{-1}$  (green) at room temperature in air. Orange symbols correspond to images showing the integrated sweat rate platform filled at  $1\text{ }\mu\text{L}\cdot\text{min}^{-1}$  with 0  $\mu\text{L}$  (empty, circle), 11  $\mu\text{L}$  (partially filled, diamond) and 25.5  $\mu\text{L}$  (completely filled, square) of liquid.

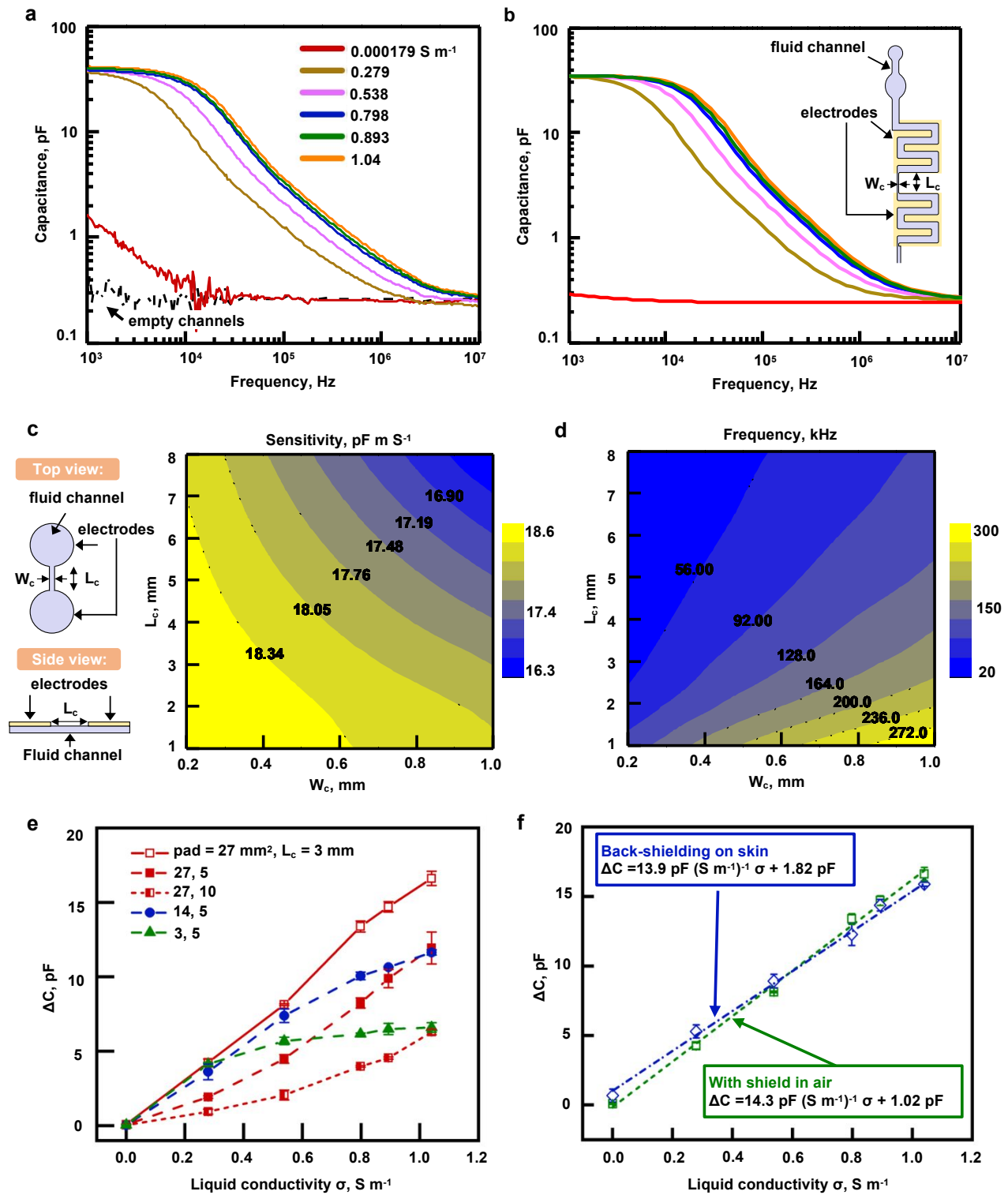


**Figure 3. Geometry optimization and benchtop evaluation of sweat conductivity channels and electrodes**

- a. Typical capacitance spectra for a sweat conductivity sensor comprising a pair of coplanar electrodes integrated with microfluidic systems (pad area  $p=27 \text{ mm}^2$ , channel length  $L_c=3 \text{ mm}$ ) at room temperature in air. The initially empty channels (dashed black line) are filled with different conductive solutions (solid colored lines) with conductivities ranging from  $0.000179$  (red line) to  $1.04 \text{ S m}^{-1}$  (orange line). Those liquids (also used for Figure 3e and f measurements) include DI water, NaCl solutions with multiple concentrations, as well as commercial artificial sweat. The capacitance behavior varies distinctively from  $2 \text{ kHz}$  to  $3 \text{ MHz}$  in response to the different conductive liquids. At a given frequency within the range of the sharp decrease of capacitance, the values recorded for different conductivities are different and thus allow a measurement of conductivity through capacitance.
- b. Corresponding FEA results of the capacitance for different conductive solutions using the sensor geometry (inset) with channel length  $L_c=3 \text{ mm}$  and channel width  $W_c=0.2 \text{ mm}$ , with same color code as in part a of this figure. The results show excellent agreement with experimental results without any parameter fitting.
- c. FEA contour of maximum sensitivity based on a parametric study of the connecting channel width  $W_c$  and length  $L_c$  (shown in the schematic on the left) between circular channels in a simplified model of the actual geometry. The size of the circular channels is adjusted to maintain a constant volume while the connecting channel dimensions vary. To maximize the sensitivity, the results suggest that the dimensions of  $W_c$  and  $L_c$  must be small.
- d. FEA contour of the value of the frequency when the sensor reaches maximum sensitivity. The connecting channel width  $W_c$  and length  $L_c$  are varied, as explained in part c of this figure. For given dimensions of the connecting channel, the sensitivity is maximum at the simulated frequency, which corresponds to ideal frequency for the measurement.
- e. Experiments showing the influence of geometry (pad size  $p$ , length of connecting channel  $l$ ) on the relationship between the capacitance difference between filled and empty channels and the conductivity of the liquid. Measurements are taken at  $25 \text{ kHz}$ , and the highest sensitivity is achieved with  $p=27 \text{ mm}^2$ ,  $l=3 \text{ mm}$  (for a total sensor size at the cm scale).
- f. Results with the final stack of materials for the sensor to be used on skin including a additional layer of PDMS (as shown in Fig. 1f) that allows for a back-shielding (shielding plane in between skin and electrodes). The difference in capacitance between filled and empty channels is linear as a function of liquid conductivity for the geometry chosen ( $p=27 \text{ mm}^2$ ,  $l=3 \text{ mm}$ ) and the influence of skin is small as shown by the difference between blue (on skin) and green (in air) curves in the presence of a shielding plane. Sensitivity on skin is  $13.9 \text{ pF (S.m}^{-1})^{-1}$ .



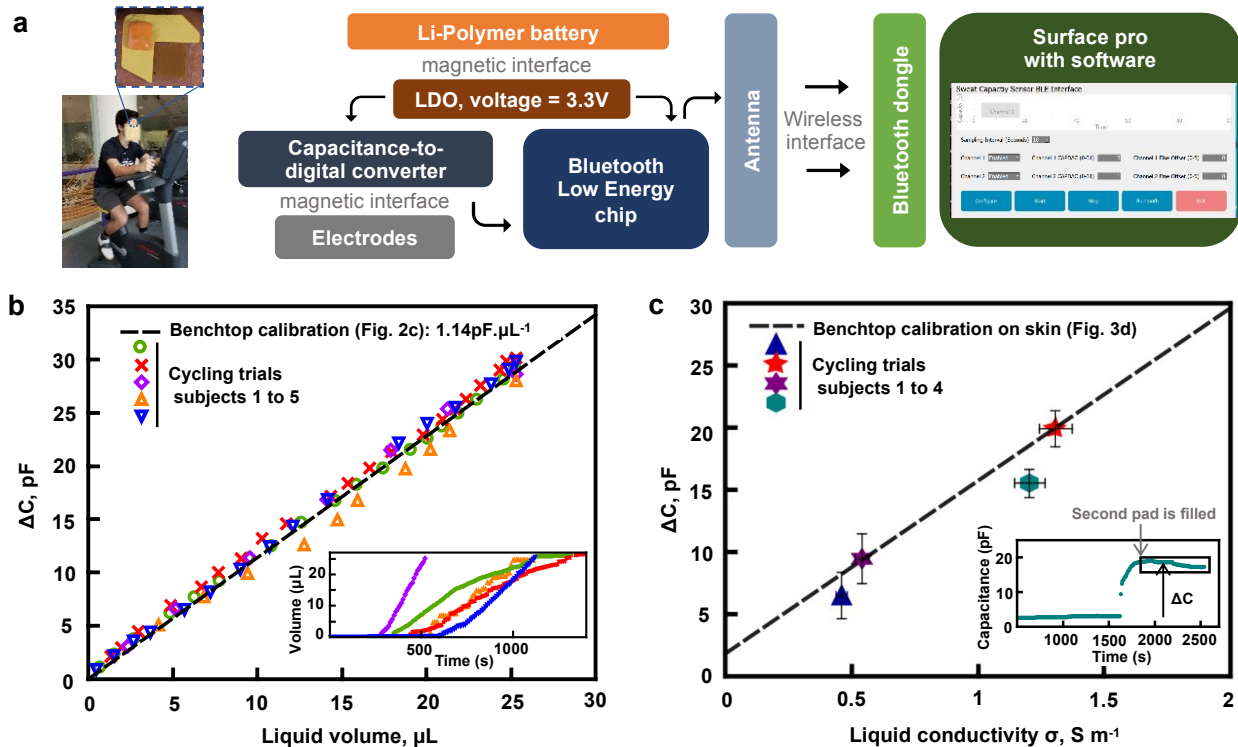


**Figure 4. Wireless on-body operation and in-situ on-body analysis of sweat collected during gym exercising.**

- Image illustrating the positioning of the device and exercising activity of the volunteers and schematic description of the system for on body-trials: battery and readout electronics that connect to the electrodes allow for real-time measurement. Transmission to the tablet occurs through a Bluetooth chip and antenna present on the electronics board, for communication to a dongle plugged into the computer via USB connection.
- Sweat rate on-body trials: difference between current capacitance and initial capacitance recorded continuously through the tablet while the actual volume present in the channels is determined through pictures taken at random intervals, for 5 subjects. The dashed black line is the benchtop calibration from Fig. 2c (no fitting parameter). Error bars are comparable to the sizes of the symbols. Inset: temporal evolution of the volume of sweat in the patch (measured through capacitance values) for all 5 subjects, with same color code as the main figure.
- Plot of sweat conductivity on-body trials: the difference between the average of the capacitance of the filled device and the initial capacitance as a function of the sweat conductivity (value at  $22^\circ\text{C}$ ). Error bars refer to the dilution precision on the X axis and to

both the standard variation within the trial and systematic error on the Y axis. Inset: temporal evolution of the measured capacitance as a function of time for one trial, illustrating how  $\Delta C$  is measured.

Stick-on electrodes capacitively coupled to single-use microfluidic channels enable contactless analysis of sweat in a soft wearable format with real-time wireless data collection.

